RSC Advances

PAPER

View Article Online
View Journal | View Issue

Cite this: *RSC Adv.*, 2020, **10**, 18245

Bilayered microelectrodes based on electrochemically deposited MnO_2/polypyrrole towards fast charge transport kinetics for micro-supercapacitors†

Waqas Ali Haider,[a] Liang He,[*a] Hameed A. Mirza,[bc] Muhammad Tahir,[a] Aamir Minhas Khan,[d] Kwadwo Asare Owusu,[a] Wei Yang,[a] Zhuqing Wang[e] and Liqiang Mai[*a]

Micro-supercapacitors (MSCs) are promising power solution facilities for miniaturized portable electronic devices. Microfabrication of on-chip MSC with high specific capacitance and high energy density is still a great challenge. Herein, we report a high-performance MnO_2/polypyrrole (PPy) microelectrode based MSC (MnO_2/PPy-MSC) by modern micromachining technology. Interdigital Au micro current collectors were obtained by photolithography, physical vapor deposition and lift off. A layer of PPy was electrochemically deposited on Au current collectors followed by deposition of urchin-like MnO_2 micro/nanostructures. The electrochemical performance of MnO_2/PPy-MSC was explored employing $LiClO_4$/PVA gel electrolyte. The assembled MSC demonstrated a high areal capacitance of 13 mF cm^{-2}, an energy density of 1.07 × 10^{-3} mW h cm^{-2} and a power density of 0.53 mW cm^{-2}. In addition, the MnO_2/PPy-MSC showed an improved cycling stability, retaining 84% of the initial capacitance after 5000 CV cycles at a scan rate of 500 mV s^{-1}. Our proposed strategy provides a versatile and promising method for the fabrication of high-performance MSCs with large-scale applications.

Received 22nd February 2020
Accepted 18th April 2020

DOI: 10.1039/d0ra01702g

rsc.li/rsc-advances

Introduction

With the emerging trend and advancement of miniaturized portable electronics, there is an increasing demand for high-performance microscale energy storage systems with high reliability.[1] In this regard, planar micro-supercapacitors (MSCs) are beneficial power sources due to their small size, excellent rate performance and long cycling life.[2,3] MSCs are highly promising for wafer-level integration and applications in microsystems due to their great potential of bridging the gap between microbatteries and conventional supercapacitors.[4] They are capable of recharging and delivering power faster than those of microbatteries and store more energy than those of capacitors. Based on the inner energy storage phenomenon, MSCs are usually categorized into electrochemical double layer capacitors (EDLCs), and pseudocapacitors.[5] EDLC stores charge through ion adsorption/desorption while pseudocapacitor involves rapid reversible redox reaction at the electrode–electrolyte interface.

MSCs have the advantages by virtue of their distinctive interdigital structure with finger microelectrodes.[6,7] MSCs based on pseudocapacitive mechanism provide opportunity to achieve higher capacity and energy storage compared with EDLC, but lack fast charge–discharge rate. Various factors are under consideration that have potential to improve overall performance. A decrease in equivalent series capacitance (ESR) will significantly increase the specific capacitance and endow MSC with a high specific energy.[8] The ESR can be decreased by fabricating a device with small migration distance of ions that can be controlled by adjusting the width of microelectrodes and the insulating gap.[9] The energy and power densities can be considerably improved with reduced ESR and improved electrical conductivity.[10,11] Enormous amount of researches have been done in this context with different active materials and techniques.

Conducting polymers and metal oxides/hydroxides have gained attention as the auspicious electrode materials for electrochemical energy storage.[12,13] These materials show pseudocapacitive behavior in MSCs, offering a way for achieving high energy density without compromising their high power

[a]State Key Laboratory of Advanced Technology for Materials Synthesis and Processing, Wuhan University of Technology, Wuhan 430070, Hubei, China. E-mail: hel@whut.edu.cn; mlq518@whut.edu.cn

[b]Department of Chemistry, York University, Toronto M3J 1P3, Ontario, Canada

[c]A.S. Chemical Laboratories Inc., Concord L4K 4M4, Ontario, Canada

[d]Department of Electrical Engineering and Computer Science, York University, Toronto M3J 1P3, Ontario, Canada

[e]Graduate School of Engineering, Tohoku University, Sendai 980-8579, Japan

† Electronic supplementary information (ESI) available. See DOI: 10.1039/d0ra01702g

density.[14] Among conducting polymers, polypyrrole (PPy) is considered highly promising owing to its high electrical conductivity, easy production and high chemical stability.[15] However, due to the polymeric nature and structural properties of PPy, the problems associated with stability and deterioration in cycling life over long-term charge–discharge hinder its large-scale applications.[16,17] The expedient morphology of metal oxides possesses high performance due to their high electrochemical activity but they have the problem of aggregation.[18] Structured PPy film significantly restricts the aggregation of metal oxides in the production of active electrode material.[19] Manganese dioxide (MnO_2) has been explored as an electrochemically active transition metal oxide with high theoretical specific capacitance (1370 F g^{-1}), low cost and environmental friendliness.[20,21] Although, its practical applications with high power density are limited due to its poor electrical conductivity ($\sim 10^{-7}$ S cm^{-1}) at room temperature.[22,23] Various composites based on MnO_2 have been developed to yield high electrochemical performance. MnO_2-based supercapacitors exhibit high electrical conductivity by compositing with graphene,[24,25] highly conductive Zn_2SnO_4 (ZTO) nanowires,[26] carbon nanotubes,[27,28] PPy[29] and PEDOT.[30,31]

Herein, we demonstrate the fabrication of a planar MSC with stacked MnO_2/PPy microelectrodes through facile electrodeposition and study its electrochemical performance. A layer of PPy was electrochemically deposited on Au current collectors followed by electrodeposition of urchin-like MnO_2 micro/nanostructures. We employed electrodeposition method to tailor the thickness and morphology of MnO_2 decorated PPy microelectrodes by optimizing the parameters such as current density, potential and deposition time.[32–34] The electrochemical performance of MnO_2/PPy-MSC was evaluated by using $LiClO_4$/PVA gel electrolyte. Our approach provides distinct pathways for access of electrolyte and maximum charge transfer through microelectrodes, while preventing the aggregation of MnO_2. The fabricated MSC exhibits an improved specific capacitance and energy density by the virtue of highly conductive PPy and high capacitive property of MnO_2. A layer of PPy strengthens the conductivity of microelectrodes by fast electron transfer and ensures the high utilization of active material.[35] While, MnO_2 micro/nanostructures have more active sites which facilitate the fast ion diffusion and exchange at electrode–electrolyte interface, providing high capacitance.

Experimental

Microfabrication of planar MnO_2/PPy-MSC

The microfabrication procedure of MnO_2/PPy-MSC is schematically shown in Fig. 1. A silicon substrate with 300 nm SiO_2 layer was prepared using RCA cleaning process. The in-plane interdigital micropatterns of photoresist were obtained by photolithography, followed by deposition of 50 nm thick Au current collectors through physical vapor deposition (PVD) technique. Electrodeposition of MnO_2/PPy was carried out using 3-electrode system with Au current collector as working electrode, platinum (Pt) counter electrode and saturated calomel electrode (SCE) as the reference electrode. PPy was electrochemically deposited on Au current collectors using electrolyte prepared by 0.1 M pyrrole (Py), 0.5 M $LiClO_4$ and NaCl as supporting salts at a current density of 1 mA cm^{-2} for 10 min. Then urchin-like MnO_2 micro/nanostructures were deposited using the solution of 0.1 M $Mn(CH_3CO_2)_2 \cdot (H_2O)_n$ and 0.1 M Na_2SO_4. The anodic deposition was conducted at a current density of 0.2 mA cm^{-2} at room temperature for 5 min and then washed thoroughly with deionized (DI) water. Thin-film topology of microelectrodes was obtained with 1.4 μm thick layer of PPy decorated with 500 nm thick (average) MnO_2 structures. The device has 4 interdigital fingers per polarity, and the total area of microelectrodes was calculated to be 0.1066 cm^2. The total foot-print area of device is 0.1287 cm^2 as determined from the detailed dimension and configuration design shown in Fig. S1 (ESI†).

Materials characterization and electrochemical measurements

The surface morphology of microelectrodes was characterized by field emission scanning electron microscopy (FE-SEM) through JEOL JSM-7100 microscope. The thickness of active electrode material was assessed using stylus surface profiler (Bruker DEKTAK XT). X-ray diffraction (XRD) measurement was conducted to obtain crystallographic information of the electrode material by means of Bruker D8 Advance X-ray diffractometer with Cu Kα X-ray source ($\lambda = 1.5418$ Å). Raman spectra of samples were collected using Renishaw RM-1000 laser Raman microscope. Energy-dispersive X-ray spectroscopy (EDS) test was conducted for elemental analysis using Oxford IE250 system. Fourier transform infrared (FTIR) spectra of samples were acquired by 60-SXB IR spectrometer. The electrochemical tests of MSC were performed by cyclic voltammetry (CV), galvanostatic charge–discharge (GCD), and electrochemical impedance spectroscopy (EIS) using Autolab 302N.

The electrochemical performance of MSC was determined by evaluating the areal capacitance (C_a) *via* GCD using the following equation.

$$C_a = \frac{i\Delta t}{a\Delta V}\left(\text{mF cm}^{-2}\right) \quad (1)$$

where i (mA) and Δt (s) are the discharging current and time, respectively, a (cm^2) is the area of microelectrodes and ΔV (V) is the operational voltage window excluding IR drop.

The areal energy density (E_a) and power density (P_a) were evaluated by following equations:

$$E_a = \frac{C_a(\Delta V)^2}{7200}\left(\text{mW h cm}^{-2}\right) \quad (2)$$

$$P_a = \frac{E_a \times 3600}{\Delta t}\left(\text{mW cm}^{-2}\right) \quad (3)$$

ESR of device was estimated from discharge curve by using the following equation:

$$\text{ESR} = \frac{V_{\text{drop}}}{2I}\left(\Omega\ \text{cm}^2\right) \quad (4)$$

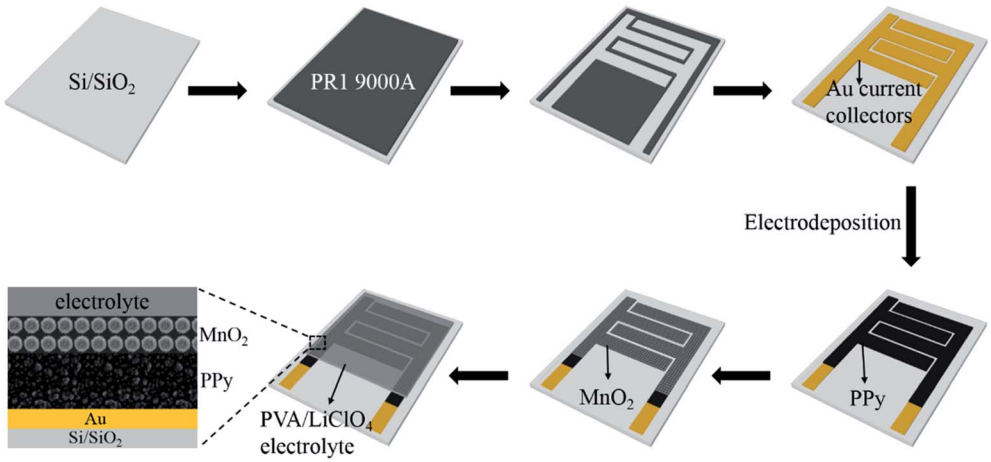

Fig. 1 Schematic illustration of fabrication of MnO_2/PPy-MSC.

where V_{drop} is the voltage drop in the beginning of discharge curve and I is the constant discharge current.

Results and discussion

SEM image (Fig. 2a) reveals the cauliflower-like structure, indicating the incorporation of electrochemically deposited PPy. A layer of PPy participates actively in electron transfer from microelectrodes to current collectors. A fine PPy layer can be obtained by optimizing the deposition time and other parameters. Fig. 2b shows the urchin-like MnO_2 structures uniformly deposited onto the PPy layer, and the size of MnO_2 structures lies in 500 nm to 1 μm. Usually MnO_2 offers high ion diffusion but due to its poor electrical conductivity the ions interaction is limited only to the near surface. It can be observed from the morphology that MnO_2 micro/nanostructures offer large intercalation channels and more diffusion pathways for redox reaction. MnO_2 micro/nanostructures hold the PPy chains from breaking and create additional active sites for the transfer of ions and electrons during charge and discharge processes. Fig. S2(a and b, ESI†), respectively shows the optical and SEM images of microelectrodes with no obvious defects. The microelectrodes are not broken or cracked, thus physical practicability of fabrication process is confirmed. The energy-dispersive spectroscopy (EDS) test was performed for elemental analysis and to estimate the relative abundance of elements. Fig. S3 (ESI†) shows the EDS mapping of MnO_2/PPy microelectrode and the elements of manganese (Mn), oxygen (O), carbon (C) and nitrogen (N) are uniformly dispersed, confirming the existence of MnO_2 and PPy.

The crystal structure of MnO_2/PPy microelectrodes was characterized by XRD, as shown in Fig. 3a. It is observed that the sharp diffracting peaks indicate high degree of crystallinity and are indexed to tetragonal structure of MnO_2 phase (JCPDS card no. 01-081-2261, $a = b = 4.404$ Å, and $c = 2.876$ Å). The crystal structure in correspondence with the morphology shows that the deposited MnO_2 exhibits high diffusivity and capacitive properties. The XRD pattern also shows the amorphous nature of composite as it exhibits a broad peak at ~21° in XRD diffractogram.[36] The broadening of peak is due to the scattered X-

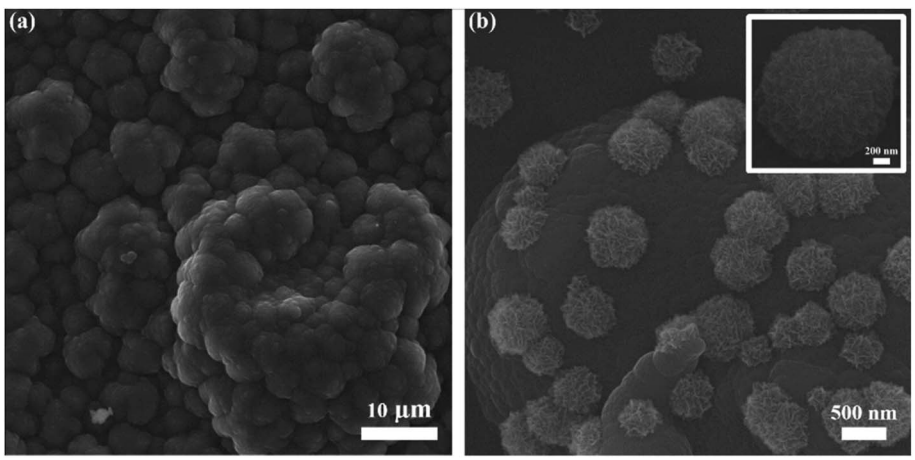

Fig. 2 SEM images of (a) electrochemically deposited PPy, (b) MnO_2 micro/nanostructures deposited onto the PPY and inset is the magnified SEM image of MnO_2 microstructure.

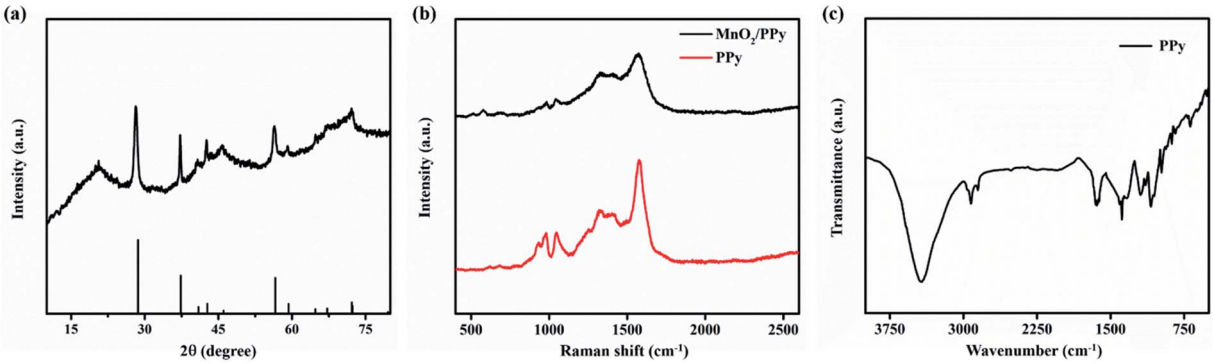

Fig. 3 (a) XRD pattern of MnO_2/PPy, (b) Raman spectra of PPy and MnO_2/PPy, and (c) FTIR spectrum of PPy.

rays from the interplanar spacing of polymer chains and could be ascribed to the amorphous PPy.[37] Fig. 3b shows the Raman spectra of PPy and MnO_2/PPy. The spectrum of MnO_2/PPy at 1570 cm^{-1} corresponds to the C=C symmetry stretching of oxidized PPy. The peaks at 1326 and 1400 cm^{-1} are attributed to pyrrole ring of PPy stretching. The characteristic peaks of PPy at 1047, 980 and 932 cm^{-1} show the C–H in-plane deformation and the ring deformation due to bipolaron and polaron species, respectively.[38,39] Finally, the peaks observed at 510 and 576 cm^{-1} show the vibration of Mn–O lattice resulting from the deposition of MnO_2 onto PPy microstructure matrix. Fig. 3c shows the Fourier transform infrared (FTIR) spectrum ranging from 3900 cm^{-1} to 400 cm^{-1} that confirms the species of as-electrodeposited PPy. The broad signal with high intensity at 3425 cm^{-1} is ascribed to N–H stretching vibration and the peak at 2923 cm^{-1} could be referred to C–H stretching owing to the smaller mass of H atom.[40,41] The characteristic peak in diagnostic region at 1651 cm^{-1} is referred to stretching vibrations of C=C bonds of PPy rings.[42] Other transmittance peaks in finger print region of C–N (1384 cm^{-1}), C–C (1195 cm^{-1}), N–H (1090 cm^{-1}) and C–H (935, 841, 690 cm^{-1}) can be observed, confirming the formation of PPy.[43,44]

The MnO_2/PPy-MSC was assembled by applying 1 M $LiClO_4$/PVA gel electrolyte and tested for electrochemical performance from CV, GCD and EIS with 2-electrodes system. Fig. 4a displays the CV curves of MnO_2/PPy-MSC under 0–0.8 V at different scan rates. The quasi-rectangular CV curve shows a successive redox reaction on the electrode surface that corresponds to the capacitive properties of MnO_2. The larger enclosed area and high response current density represent the charge storage and excellent pseudocapacitive behaviour due to the synergistic effect of MnO_2 and PPy. PPy plays an important role in utilization of active electrode material for redox reaction and electron transfer. Electrochemical performance of MnO_2/PPy-MSC was further examined by performing GCD measurement at different current densities (Fig. 4b). It shows the relatively symmetric charge–discharge curve, indicating high reversibility with the characteristics of reversible redox reaction. The voltage drop of 0.029 V in the discharge curve at the current density of 0.1 mA cm^{-2} shows the smaller internal resistance of ~147 Ω cm^2 as calculated by the eqn (4). CV and GCD curves at high scan rates and current densities are shown in Fig. S4(a and b, ESI†), respectively. Fig. 4(c and d) presents the comparison of CV and GCD of MnO_2/PPy-MSC with that of MnO_2-MSC. The CV curves at 10 mV s^{-1} demonstrate significant increase in the capacitive performance of MSC with PPy as conducting layer for micro-electrode. The GCD curve at a current density of 0.2 mA cm^{-2} also shows a notable increase in the discharge time and capacitance, consequently the fabricated MSC exhibits an enhanced energy density. Moreover, the electrochemical performance of MnO_2/PPy-MSC was also compared with another device fabricated by electrodepositing PPy over the MnO_2 (PPy@MnO_2-MSC), as shown in Fig. S5(a and b, ESI†).

EIS test was performed to further investigate the resistance and kinetic process of electrode reaction. The typical Nyquist plot at open circuit voltage over a frequency ranging from 100 KHz to 0.01 Hz is shown in Fig. 5a. The impedance spectrum presents a well-defined semi-circle at real axis in a high frequency followed by a sheer graph with steep slope in low frequency Warburg region. The amplified curve in high frequency region is shown in the inset. The intercept at real axis represents the lower internal resistance of about 45 Ω and the diameter of semi-circle indicate the charge transfer resistance (R_{ct}) of 6.7 Ω caused by faradaic reaction on the electrode–electrolyte interface and interior. The vertical graph at low frequency is nearly aligned with imaginary axis and represents the ideal capacitive behavior of composite electrode due to the ion diffusion and mobility. Rate capability is significant for the evaluation of the power applications of MSC. Fig. 5b shows the specific capacitances at different corresponding current densities. The MnO_2/PPy-MSC demonstrates a rate capability of 62.2% at 1 mA cm^{-2} as compared with the capacitance at current density of 0.1 mA cm^{-2}. The percentage of capacitance retention at different current densities with corresponding IR drop is shown in Fig. S6 (ESI†). The sudden voltage drop in the discharge curve is the measure of total resistance of the MSC and is proportional to the discharge current. A smaller voltage drop at a high current density indicates low internal resistance of the tested device. The voltage drop increases at higher current density, as shown by the V_{drop} graph in Fig. 5b.

CV cycling was conducted at a higher scan rate to evaluate the stability of MnO_2/PPy-MSC. The percentage of capacitance

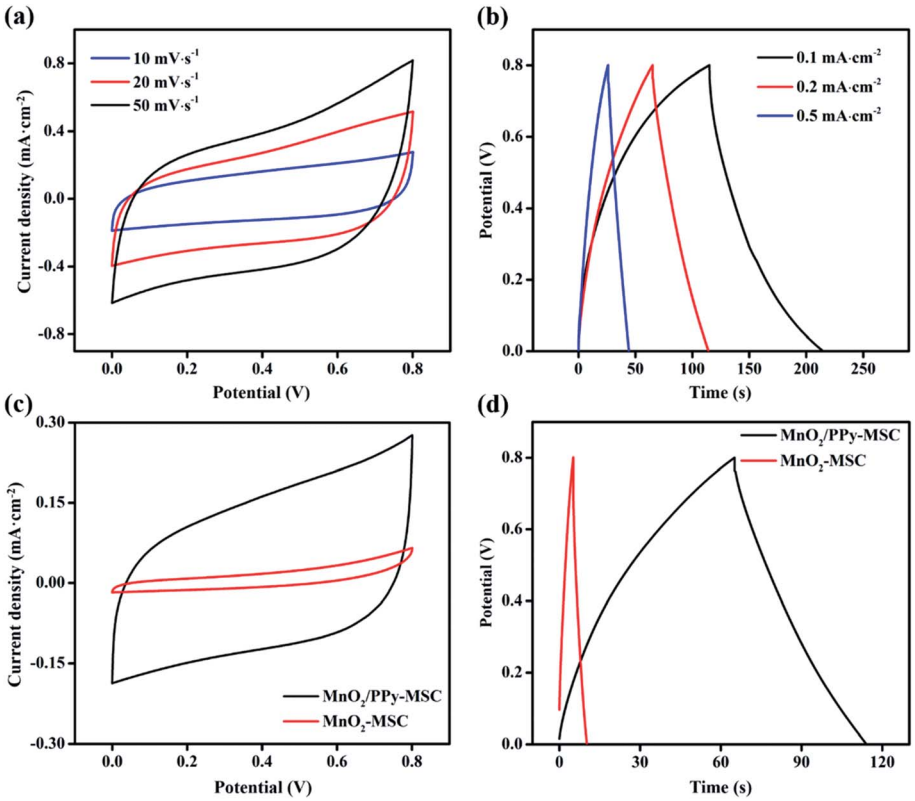

Fig. 4 (a) Cyclic voltammetry and (b) galvanostatic charge–discharge curves of MnO_2/PPy-MSC. (c) Comparison of CV and (d) GCD of MnO_2/PPy-MSC and MnO_2-MSC.

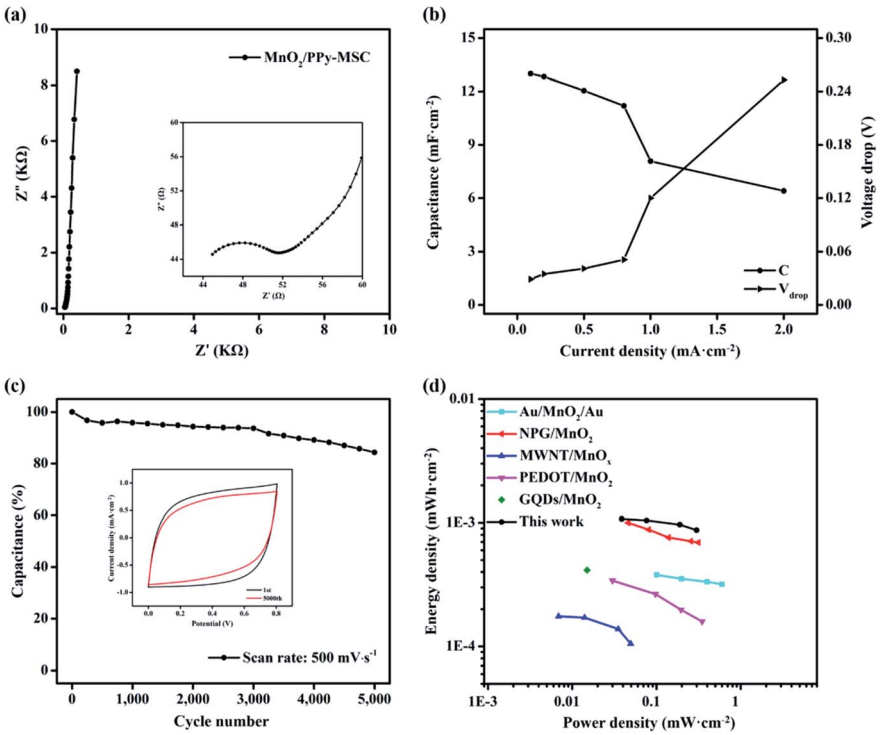

Fig. 5 (a) Nyquist plot of MnO_2/PPy-MSC, inset is the Nyquist plot in high frequency region. (b) Specific areal capacitances and corresponding voltage drops at different current densities. (c) Cycling performance of MnO_2/PPy-MSC at 0.5 V s^{-1}. (d) Ragone plot of MnO_2/PPy-MSC and analogy with other MSCs.

retained after 5000 cycles at 500 mV s^{-1} is shown in Fig. 5c. Generally, the doping and undoping of ions in polymers could cause volume change of electrode.[45] This swelling and shrinking affect the mechanical structure and eventually aggravate the electrochemical performance.[46] Usually, pure PPy presents a low stability due to the degradation of polymer chains and deterioration of electrode material during continuous CV cycles.[47,48] Herein, the inclusion of MnO_2 keeps the PPy polymer chains stable and enhances the cycling life of MSC. Consequently, 84% of actual capacitance is retained after 5000 cycles, showing improved stability and cycling performance.[49] The inset graph shows the reduction in current density and enclosed area of the 5000th CV curve during the cycling process. The specific areal energy and power densities are further determined from charge–discharge curves, Fig. 5d shows the results and Ragone plot analogy. MnO_2/PPy-MSC achieves an energy density of 1.07 $\times$ 10^{-3} mW h cm^{-2} and a power density of 0.53 mW cm^{-2}, greater than those of MSCs based on interdigital Au/MnO_2/Au,[50] nanoporous gold (NPG)/MnO_2,[51] MWNT/MnO_x,[52] Ag/PEDOT:PSS/MnO_2 (ref. 53) and graphene quantum dots/MnO_2.[54] Fig. S7 (ESI†) shows the corresponding energy and power densities at various current densities. Improved energy density is attributed to the pseudocapacitive properties of MnO_2, high electrical conductivity of PPy and the fine patterning with narrow gap between the fingers.

Conclusions

In summary, we have fabricated a distinctive on-chip micro-supercapacitor with enhanced capacitance from a trivial footprint. The fabricated MSC demonstrates improved electrochemical and mechanical performances by highly effective combination of high electrical conductivity of PPy and pseudocapacitive properties of MnO_2. PPy facilitates the fast electron transport and clearly reduce the resistance of MSC. While, MnO_2 micro/nanostructures efficiently increase the ionic penetration by creating more electrochemically active sites and thus enhance the specific capacitance. MnO_2/PPy-MSC shows an areal capacitance of 13 mF cm^{-2} in PVA/$LiClO_4$ gel electrolyte at a current density of 0.1 mA cm^{-2}. The MnO_2 micro/nanostructures deposited onto the PPy further improve the cycling stability and the MnO_2/PPy-MSC possesses 84% of capacitance after 5000 CV cycles. Cooperative action of layered MnO_2 and PPy demonstrates higher electrochemical performance than that of microelectrodes based on pristine materials. These findings promote new opportunities for polymer/metal oxide based state-of-the-art micro-supercapacitors.

Conflicts of interest

There are no conflicts to declare.

Acknowledgements

This work was supported by the State Key Laboratory of Advanced Technology for Materials Synthesis and Processing (WUT:2019-KF-5, 2019-KF-2), the National Natural Science Fund for Distinguished Young Scholars (51425204), the National Natural Science Foundation of China (51521001), the National Key Research and Development Program of China (2016YFA0202603, 2016YFA0202604), the Program of Introducing Talents of Discipline to Universities (B17034), and the Yellow Crane Talent (Science & Technology) Program of Wuhan City.

References

1 S. Wang, Z.-S. Wu, F. Zhou, X. Shi, S. Zheng, J. Qin, H. Xiao, C. Sun and X. Bao, *npj 2D Mater. Appl.*, 2018, **2**, 7.
2 D. Qi, Y. Liu, Z. Liu, L. Zhang and X. Chen, *Adv. Mater.*, 2017, **29**, 1602802.
3 S. Wang, Z.-S. Wu, S. Zheng, F. Zhou, C. Sun, H.-M. Cheng and X. Bao, *ACS Nano*, 2017, **11**, 4283–4291.
4 C. Lethien, J. Le Bideau and T. Brousse, *Energy Environ. Sci.*, 2019, **12**, 96–115.
5 Z. S. Wu, K. Parvez, X. Feng and K. Müllen, *Nat. Commun.*, 2013, **4**, 2487.
6 H. Li and J. Liang, *Adv. Mater.*, 2019, 1805864.
7 W. A. Haider, M. Tahir, L. He, W. Yang, A. Minhas-khan, K. A. Owusu, Y. Chen, X. Hong and L. Mai, *J. Alloys Compd.*, 2020, **823**, 151769.
8 L. Demarconnay, E. Raymundo-Pinero and F. Béguin, *J. Power Sources*, 2011, **196**, 580–586.
9 N. Liu and Y. Gao, *Small*, 2017, **13**, 1701989.
10 B. Mendoza-Sánchez and Y. Gogotsi, *Adv. Mater.*, 2016, **28**, 6104–6135.
11 G. Xiong, C. Meng, R. G. Reifenberger, P. P. Irazoqui and T. S. Fisher, *Electroanalysis*, 2014, **26**, 30–51.
12 M. Boota and Y. Gogotsi, *Adv. Energy Mater.*, 2019, **9**, 1802917.
13 M. Tahir, L. He, W. A. Haider, W. Yang, X. Hong, Y. Guo, X. Pan, H. Tang, Y. Li and L. Mai, *Nanoscale*, 2019, **11**, 7761–7770.
14 G. Huang, Y. Zhang, L. Wang, P. Sheng and H. Peng, *Carbon*, 2017, **125**, 595–604.
15 H. Wei, C. He, J. Liu, H. Gu, Y. Wang, X. Yan, J. Guo, D. Ding, N. Z. Shen and X. Wang, *Polymer*, 2015, **67**, 192–199.
16 J. Chen, Y. Wang, J. Cao, Y. Liu, Y. Zhou, J.-H. Ouyang and D. Jia, *ACS Appl. Mater. Interfaces*, 2017, **9**, 19831–19842.
17 M. Tahir, L. He, W. Yang, X. Hong, W. A. Haider, H. Tang, Z. Zhu, K. A. Owusu and L. Mai, *J. Energy Chem.*, 2020, **49**, 224–232.
18 K. Li, X. Liu, T. Zheng, D. Jiang, Z. Zhou, C. Liu, X. Zhang, Y. Zhang and D. Losic, *Chem. Eng. J.*, 2019, **370**, 136–147.
19 K. Li, S. Feng, C. Jing, Y. Chen, X. Liu, Y. Zhang and L. Zhou, *Chem. Commun.*, 2019, **55**, 13773–13776.
20 M. Nakayama, K. Kaneshige and K. Komine, *ECS Trans.*, 2017, **75**, 19.
21 L. He, H. Liu, W. Luo, W. Zhang, X. Liao, Y. Guo, T. Hong, H. Yuan and L. Mai, *Appl. Phys. Lett.*, 2019, **114**, 223903.
22 D. Bélanger, L. Brousse and J. W. Long, *Electrochem. Soc. Interface*, 2008, **17**, 49.
23 C. M. Julien and A. Mauger, *Nanomaterials*, 2017, **7**, 396.
24 L. Peng, X. Peng, B. Liu, C. Wu, Y. Xie and G. Yu, *Nano Lett.*, 2013, **13**, 2151–2157.

25 Z. Fan, J. Yan, T. Wei, L. Zhi, G. Ning, T. Li and F. Wei, *Adv. Funct. Mater.*, 2011, **21**, 2366–2375.
26 L. Bao, J. Zang and X. Li, *Nano Lett.*, 2011, **11**, 1215–1220.
27 P. Xu, B. Wei, Z. Cao, J. Zheng, K. Gong, F. Li, J. Yu, Q. Li, W. Lu and J.-H. Byun, *ACS Nano*, 2015, **9**, 6088–6096.
28 L. Sun, X. Wang, K. Zhang, J. Zou and Q. Zhang, *Nano Energy*, 2016, **22**, 11–18.
29 A. Bahloul, B. Nessark, E. Briot, H. Groult, A. Mauger, K. Zaghib and C. Julien, *J. Power Sources*, 2013, **240**, 267–272.
30 P. Tang, L. Han and L. Zhang, *ACS Appl. Mater. Interfaces*, 2014, **6**, 10506–10515.
31 Y. Chen, J. Xu, Y. Yang, Y. Zhao, W. Yang, X. Mao, X. He and S. Li, *Electrochim. Acta*, 2016, **193**, 199–205.
32 S. Gao, L. Zhang, Y. Qiao, P. Dong, J. Shi and S. Cao, *RSC Adv.*, 2016, **6**, 58854–58861.
33 M. Ghosh, V. Vijayakumar, R. Soni and S. Kurungot, *Nanoscale*, 2018, **10**, 8741–8751.
34 R. Della Noce, S. Eugénio, T. Silva, M. Carmezim and M. Montemor, *RSC Adv.*, 2017, **7**, 32038–32043.
35 X. Fan, X. Wang, G. Li, A. Yu and Z. Chen, *J. Power Sources*, 2016, **326**, 357–364.
36 M. Mahmoudian, Y. Alias, W. Basirun and M. Ebadi, *Appl. Surf. Sci.*, 2013, **268**, 302–311.
37 V. Shanthala, S. Shobha Devi and M. Murugendrappa, *J. Asian Ceram. Soc.*, 2017, **5**, 227–234.
38 X. Liu, T. Qian, N. Xu, J. Zhou, J. Guo and C. Yan, *Carbon*, 2015, **92**, 348–353.
39 Y. Liu, J. Zhou, J. Tang and W. Tang, *Chem. Mater.*, 2015, **27**, 7034–7041.
40 N. Ilicheva, N. Kitaeva, V. Duflot and V. Kabanova, *ISRN Polym. Sci.*, 2012, **2012**, 320316.
41 Y. Zhou, P. Wang, M. Hu and X. Tian, *Electrochim. Acta*, 2017, **249**, 290–300.
42 Y. Jia, P. Xiao, H. He, J. Yao, F. Liu, Z. Wang and Y. Li, *Appl. Surf. Sci.*, 2012, **258**, 6627–6631.
43 X. Zhang, J. Wang, J. Liu, J. Wu, H. Chen and H. Bi, *Carbon*, 2017, **115**, 134–146.
44 Z. Chen, W. Liao and X. Ni, *Chem. Eng. J.*, 2017, **327**, 1198–1207.
45 G. A. Snook, P. Kao and A. S. Best, *J. Power Sources*, 2011, **196**, 1–12.
46 V. Khomenko, E. Frackowiak and F. Beguin, *Electrochim. Acta*, 2005, **50**, 2499–2506.
47 H. A. A. Bashid, H. N. Lim, S. Kamaruzaman, S. A. Rashid, R. Yunus, N. M. Huang, C. Y. Yin, M. M. Rahman, M. Altarawneh and Z. T. Jiang, *Nanoscale Res. Lett.*, 2017, **12**, 246.
48 L.-l. Jiang, X. Lu, C.-m. Xie, G.-j. Wan, H.-p. Zhang and T. Youhong, *J. Phys. Chem. C*, 2015, **119**, 3903–3910.
49 C. Ng, H. Lim, Y. Lim, W. Chee and N. Huang, *Int. J. Energy Res.*, 2015, **39**, 344–355.
50 H. Hu, Z. Pei, H. Fan and C. Ye, *Small*, 2016, **12**, 3059–3069.
51 X. Shi, Z. Zeng, C. Liao, S. Tao, E. Guo, X. Long, X. Wang, D. Deng and Y. Dai, *J. Alloys Compd.*, 2018, **739**, 979–986.
52 G. Lee, D. Kim, J. Yun, Y. Ko, J. Cho and J. S. Ha, *Nanoscale*, 2014, **6**, 9655–9664.
53 Z. Yu, C. Li, D. Abbitt and J. Thomas, *J. Mater. Chem. A*, 2014, **2**, 10923–10929.
54 B. Shen, J. Lang, R. Guo, X. Zhang and X. Yan, *ACS Appl. Mater. Interfaces*, 2015, **7**, 25378–25389.